Plasmonics (2014) 9:261–272
DOI 10.1007/s11468-013-9619-6

Interfacial Susceptibilities in Nanoplasmonics via Inversion of Fresnel Coefficients

Rémi Lazzari · Ingve Simonsen · Jacques Jupille

Received: 25 April 2013 / Accepted: 2 September 2013 / Published online: 4 October 2013

Abstract The reflection coefficients of a nanoparticle film are driven to a large extent by perpendicular and parallel interfacial susceptibilities that have the meaning of "dielectric thicknesses" which combine the actual geometry of the film and its dielectric properties. The direct determination of these parameters faces the long-standing issue of the derivation of complex optical constants from Fresnel coefficients via a unique spectroscopic measurement. The present work sets up an iterative algorithm based on inversion of the reflection coefficients recorded in the UV–visible range for two polarization states *s* and *p* and Kramers–Kronig (KK) analysis. To calculate the KK integrals over a limited energy window, the strategy was to complement measurements by spectra calculated in the framework of the spheroidal dipole approximation. The algorithm has been successfully tested on synthetic data of differential reflectivity for supported truncated spheres. These were chosen to span different dielectric behaviors, involving (a) for the particles, metals whose optical response is dominated by plasmonic excitations with a noticeable Drude behavior (Ag and Au) and (b) for the substrate, either nonabsorbing wide bandgap (alumina) or semiconducting (zincite and titania) oxides. Unlike the thin plate model, the approach was proven to apply to "dielectric thicknesses" of several tens of nanometres in cases in which, even for geometric sizes of the order of the nanometer, the classical long-wavelength dielectric approximation fails because of strong plasmon resonances. Therefore, the disentanglement of dielectric behaviors along the parallel and perpendicular directions simplifies the understanding on the interface polarization process by removing substrate contribution. The present work that deals with plasmonics in nanoparticles can be easily generalized to different morphologies as well as to other combinations of Fresnel coefficients.

Keywords Plasmon · Nanoparticles · Dielectric constant · Interface susceptibilities · Polarizability · Surface differential reflectivity spectroscopy · Film

R. Lazzari (✉) · J. Jupille
Institut des NanoSciences de Paris, CNRS UMR 7588
UPMC University Paris 06 and CNRS, 4 Place Jussieu,
75252 Paris Cedex 05, France
e-mail: remi.lazzari@insp.jussieu.fr

J. Jupille
e-mail: jacques.jupille@insp.jussieu.fr

I. Simonsen
Department of Physics, Norwegian University of Science and Technology (NTNU), 7491 Trondheim, Norway
e-mail: ingve.simonsen@phys.ntnu.no

Introduction

The capability of light to characterize, via plasmon excitation, metallic nano-objects whose size is much smaller than the wavelength, which is at the heart of the recent development of nanoplasmonics [1], has constantly inspired the development of modelings [2–4]. Light has the advantage of being a nondestructive tool that can be operated either in vacuum or in gaseous and liquid environments. Sensitive to particle shape and interactions with both support and neighboring particles, nanoplasmonics is of great relevance to determine the morphology of supported metal clusters via the description of representative average objects [3–7]. Light is also currently used to probe physical phenomena such as growth [6–8], adsorption [9], core–shell segregation [10], and particle melting [11]. In contrast with free-standing objects, both because of the truncated shape of

the supported particle and of its contact with the dissimilar medium of the support, a crucial aspect of the modeling is the description of the anisotropy of the optical response that is accounted for by a series of multipolar components [3, 4] for sub-wavelength particles. In line with earlier demonstrations made on the basis of the thin plate model in the long-wavelength regime (or three phase model), a general picture emerges in which the reflection coefficients of a in-plane isotropic surface film are driven to a large extent by parallel and perpendicular "dielectric thickness" components which combine the actual geometry of the film and its dielectric properties [5, 12–17]. For cases in which the involved dimensions are much smaller than the wavelength, a generalization of these approaches to any geometry was developed by Bedeaux and Vlieger [3, 18, 19] in terms of excess fields and parallel $\gamma(\omega)$ and perpendicular $\beta(\omega)$ frequency-dependent interfacial susceptibilities (IS). However, the blurring of the optical response by the substrate contribution [20] complicates dramatically the direct reading of the optical parameters of the film itself in a reflectivity measurement, not to mention the polarization intertwining of the parallel and perpendicular directions. Therefore, the knowledge on those anisotropy-sensitive parameters is a challenging issue for optical analysis since they contain all the physics of the polarization process of the interface.

The present work aims at deriving the interfacial susceptibilities $\gamma(\omega)$, $\beta(\omega)$ from the simultaneous surface differential reflectivity spectroscopy (SDRS) measurements of reflection coefficients in p and s polarizations on a finite energy domain. SDRS is an appropriate method to unravel the optical behavior of supported thin films with in situ and online capabilities. The surface sensitivity due to differential measurements [21] favors its use in the studies of thin film growth and of adsorption processes [22, 23]. For instance, plasmon excitations in metallic nanosized islands [6, 24–26] or optical transitions in complex organic molecular architecture [20, 27, 28] appear as bands which profiles depends not only on the electronic structure of the deposit but also on its morphology and on the substrate contributions. SDRS spectra of supported nanoparticles represented by either truncated spheres or spheroids were previously successfully fitted at multipolar order [6, 7, 24, 26, 29–33], and shape-driven multipolar absorption modes [31, 32, 34, 35] were described on the basis of the concepts of IS. The soundness of the theory allowed to draw a close parallel between electron energy loss spectra and optical responses of plasmon resonances of silver films supported on semiconductors and oxides [36]. The limits of the approach are (a) to depend on the shape chosen for the supported particles, (b) to rely on complex modeling at multipolar order, and (c) to use temperature- and size-dependent corrections of the material dielectric functions [6, 26, 30, 33]. Qualitative and direct information could be gained from an inverse approach by extracting from measurements the dielectric contribution induced by the film alone [37, 38] (i.e., the IS). However, the direct determination of the "dielectric thicknesses" faces the long-standing problem [39] of the derivation of complex optical constants from Fresnel coefficients via unique spectroscopic measurements. Beyond combination of different independent measurements to constrain the solution [38–40] (such as measurements of reflection/transmission/absorption/ellipsometric coefficients at various incident angles and/or polarization), the single spectroscopic approach can be supplemented by an analysis based on the celebrated Kramers–Kronig (KK) relations [41] which link real and imaginary parts of the sought response function. The difficulty is to match the finite energy bandwidth in which data are recorded to the infinite range on which KK integrals are defined. The only way to overcome the nonlocal character of the KK transform is to introduce some physical input or guess for the missing part of the signal [41]. For thin continuous films, strategies have been based on estimates of the dielectric function at the boundaries that can be derived either as static values [37, 42, 43], or at one or several points to design a single/multiple subtractive KK analysis [38, 44, 45], or via a fit to an "educated guess" of the solution [39, 46]. However, in the case of supported particles, the problem is more stringent since the IS response functions which scale with the object polarizabilities depend on the morphology of the interface and are not isotropic. This is fairly well illustrated by comparing IS of a floating layer of noninteracting full spheres [47] $\gamma(\omega) = \beta(\omega) = t[\epsilon(\omega)-1]/[\epsilon(\omega)+2]$ with IS of a thin continuous layer [3] $\gamma(\omega) = t[\epsilon(\omega)-1]$, $\beta(\omega) = t[1-1/\epsilon(\omega)]$ with the same dielectric function $\epsilon(\omega)$ and thickness t. For a Drude metal $\epsilon(\omega) = \epsilon_\infty - \omega_p^2/\omega^2$, both the static IS at $\omega = 0$ (and therefore the layer conductivity) and the high frequency limit differ between the two cases.

The suggestion for supported nanoparticles is to set up an iterative algorithm based on KK relations complemented by a fit of the spectra with a basic model of spheroid in the dipole approximation [3, 48–50] that is expected to grasp the missing information while the algorithm restores the main polarization physics of the islands. The approach is tested on synthetic data involving metals with plasmonic resonances in the UV–visible range (Ag and Au) supported on nonabsorbing (alumina) and absorbing (titania and zincite) oxide substrates.

Thin Film Fresnel Coefficients as Functions of Interfacial Susceptibilities

Consider an incident plane wave shining a substrate 2 from a medium 1 (herein assumed to be vacuum) at an angle of incidence θ_0 relative to the surface normal. The discussion

is restricted to in-plane isotropic interface between nonmagnetic media characterized by their bulk dielectric constants $\epsilon_{1,2}$ or refractive indexes $n_{1,2} = \sqrt{\epsilon_{1,2}}$. When the interface between them deviates from a sharp boundary as in the cases of either roughening or film made of nanoparticles, the calculation of the Fresnel linear optical coefficients becomes no longer straightforward as it depends on the local interfacial topography in the dielectric sense. Bedeaux and Vlieger [3] developed a full theoretical framework to describe the optical response of interfacial layer in which typical in-plane correlation length and thickness are much smaller than the wavelength λ of the incident light. Their modeling is based on special boundary conditions at the interface between the bulk media and involves the integral along the surface normal of the electromagnetic fields in excess to the sharp case. Similar results can be obtained by introducing singular fields at the dividing surface [3, 18, 51, 52]. The integrated excess fields are related to the bulk fields extrapolated to the surface by constitutive relations involving IS of first (γ, β) and second-order (δ, τ). More precisely, γ (respectively β) relates the integrated excess of the parallel polarization density to the average of the parallel (respectively perpendicular) components of the extrapolated bulk electric (respectively displacement) fields. For continuous films of thickness t, the "optical thicknesses" γ, β are given by

$$\gamma = t(\epsilon_2 - \epsilon_1), \quad \beta = t(1/\epsilon_1 - 1/\epsilon_2), \tag{1}$$

while for sub-wavelength islands, as in the present case:

$$\gamma = \rho \left\langle \alpha_{\parallel} \right\rangle, \quad \beta = \rho \left\langle \alpha_z \right\rangle / \epsilon_1 \tag{2}$$

ρ are the density of nanoparticles, and $\left\langle \alpha_{\parallel} \right\rangle$, $\langle \alpha_z \rangle$ is the average island polarizabilities parallel and perpendicular to the surface [3, 19, 53, 54]. Second-order IS δ, τ were also introduced to feature the nonlocal link between the fields due to the arbitrary choice of the dividing surface [3, 19]. Shifting the polarization density inside the layer leads to a coupling to the field at the original position, but the contribution is of the order of t/λ compared to the first-order term. Having sizable effects in media with low dielectric constant [3, 19], they contribute marginally to the response of metal particles (section "Synthetic Data of SDRS: Limits of Long-Wavelength Approximation and SDA Fits") and were therefore ignored in what follows.

By using the modified boundary conditions that include γ, β, the Fresnel reflection amplitudes for the two polarizations s, p are given by

$$r_s = \frac{n_1 \cos\theta_0 - n_2 \cos\theta_t + i(\omega/c)\gamma}{n_1 \cos\theta_0 + n_2 \cos\theta_t - i(\omega/c)\gamma} \tag{3}$$

$$r_p = \frac{(n_2 \cos\theta_0 - n_1 \cos\theta_t)[1 - (\omega/2c)^2 \epsilon_1 \gamma\beta \sin^2\theta_0] - i(\omega/c)\gamma \cos\theta_0 \cos\theta_t + i(\omega/c) n_1 n_2 \epsilon_1 \beta \sin^2\theta_0}{(n_2 \cos\theta_0 + n_1 \cos\theta_t)[1 - (\omega/2c)^2 \epsilon_1 \gamma\beta \sin^2\theta_0] - i(\omega/c)\gamma \cos\theta_0 \cos\theta_t - i(\omega/c) n_1 n_2 \epsilon_1 \beta \sin^2\theta_0}$$

where θ_t is the complex transmitted angle given by the Snell–Descartes law: $n_1 \sin(\theta_0) = n_2 \sin(\theta_t)$; ω is the optical angular frequency; $\omega/2\pi$ is the frequency; and $\hbar\omega$ is the photon energy. The incident wave vector modulus is given by the vacuum dispersion relation $k = 2\pi/\lambda = \omega/c$, where c is the speed of light. The dependence on the frequency $\omega/2\pi$ of all the quantities is implicit in the above equations. Fresnel's formulae for a flat interface are recovered by setting all IS to zero. The dependence of r_s on γ only reflects the excitation of the interface by the parallel component of the electric field, while the $p-$polarized light probes both parallel and perpendicular directions. Of course, the only experimentally accessible parameters are the reflection coefficients in energy:

$$\mathcal{R}_s = |r_s|^2, \quad \mathcal{R}_p = |r_p|^2 \tag{4}$$

Equation 3 and a fortiori $\mathcal{R}_{s,p}$ are nonlinear functions of the complex interfacial susceptibilities γ, β. Not speaking about the mixing of excitations along the parallel and perpendicular directions in p–polarization, the various substrate and film contributions are quite entangled in the reflection coefficients through a cross coupling between the real and imaginary parts of the IS and the substrate dielectric constant.

The situation simplifies somehow for differential reflectivity in the long-wavelength regime where $2\pi/\lambda|\gamma, \beta| = \omega/c|\gamma, \beta| \ll 1$. A first-order expansion of the squared moduli [18, 36] of Eq. 3 yields

$$\frac{\Delta\mathcal{R}_s}{\mathcal{R}_s} = 4\frac{\omega}{c} n_1 \cos\theta_0 \mathrm{Im}\left[\frac{\gamma}{\epsilon_2 - \epsilon_1}\right]$$
$$\frac{\Delta\mathcal{R}_p}{\mathcal{R}_p} = 4\frac{\omega}{c} n_1 \cos\theta_0 \mathrm{Im}\left[\frac{(\epsilon_2 - \epsilon_1 \sin^2\theta_0)\gamma - \epsilon_2^2 \epsilon_1 \sin^2\theta_0 \beta}{(\epsilon_2 - \epsilon_1)(\epsilon_2 \cos^2\theta_0 - \epsilon_1 \sin^2\theta_0)}\right] \tag{5}$$

For a nonabsorbing substrate $\mathrm{Im}(\epsilon_2) = 0$, the optical response is governed only by optical absorption inside the layer itself, and the SDRS spectra can be directly inverted to obtain the imaginary parts of the interfacial susceptibilities. Differential reflectivity formulae analogous to Eq. 5 have been derived over years by several authors [5, 12–16] using concepts of parallel and perpendicular "dielectric thicknesses" analogous to the IS that are used herein [3, 18]. Drude [12] has justified the elliptic polarization upon

reflection on a rough transition layer by the lack of "discontinuity in Nature." Later, this local and isotropic approach was generalized by McIntyre and Aspnes [5] through a long-wavelength expansion of the thin plate model. Digman and Moskovits introduced thereafter anisotropic dielectric layer treated as an uniaxial medium to uncouple the parallel and perpendicular dielectric behavior in the SDRS formulae [13, 14]. In the context of the electromagnetic modeling of the surface of metals, Bagchi et al. [15] developed a perturbation formalism of the Fresnel case to handle the reflection of light at the metal/vacuum interface in terms of frequency-dependent quantities called Λ_x and Λ_z which have the dimension of a length. At the same time, Feibelman (ref. [16] and references therein) developed a microscopic theory of electron behavior upon irradiation at metal surfaces. He introduced two complex lengths $d_\parallel$ and $d_\perp$ which measure the position of the interface in the electromagnetic point of view and the centroid of the induced charge. He related them to the reflection coefficients through formulae equivalent to Eq. 5. However, although it has not been stressed so much in all these works, the approaches rely in one way or the other onto the long-wavelength limit *in the dielectric meaning* and not *in the geometrical meaning* as with the concepts of excess fields and IS of Bedeaux and Vlieger [3]. The thin plate expansion of McIntyre and Aspnes [5, 13, 14] is accurate when the phase shift of the beam across the thin film is much smaller than one i.e. $\frac{2\pi}{\lambda} n_2 \cos(\theta_t) d \ll 1$. In papers of Bagchi et al. [15] and Feibelman [16], this assumption is hidden into either the perturbation formalism or the expansion that is used. However, as shown in (section "Thin Film Fresnel Coefficients as Functions of Interfacial Susceptibilities"), the long-wavelength approximation may fail even for well subwavelength surface region because of dielectric blowup or resonance effects such as plasmon absorptions in nano-sized particles.

Inversion Algorithm of Optical Data Based on Kramers–Kronig Transform

An inversion procedure based on Eqs. 3–4 is in principle possible by linking the real and imaginary part of $\gamma(\omega)$ (and also $\beta(\omega)$) through Kramers–Kronig (KK) relations:

$$\begin{aligned} \mathrm{Re}[\gamma(\omega)] &= \frac{2}{\pi}\wp\int_0^{+\infty} d\omega' \frac{\omega' \mathrm{Im}[\gamma(\omega')]}{\omega'^2-\omega^2} \\ \mathrm{Im}[\gamma(\omega)] &= -\frac{2}{\pi}\omega\wp\int_0^{+\infty} d\omega' \frac{\mathrm{Re}[\gamma(\omega')]}{\omega'^2-\omega^2} \end{aligned} \tag{6}$$

where $\wp$ is the Cauchy principal part of the integral. The IS $\gamma(\omega)$, $\beta(\omega)$ are indeed the Fourier transform of real causal function response [3, 18, 41]. In the case of thin continuous films (Eq. 1), this results obviously from the KK properties of the layer dielectric constant itself $\epsilon(\omega)$ or of its loss function $1/\epsilon(\omega)$. For island films (Eq. 2), the polarizability tensor, as a causal linear response coefficient, obeys the above transform. In passing, by definition [3], $\gamma(\omega)$ includes the divergence due to the layer conductivity, if any.

Knowing the dielectric constant of the substrate and the experimental reflection coefficients in *s*, *p*-polarizations (from a SDRS measurement for instance), Eqs. 3–4 can be inverted in the variables $\mathrm{Im}[\gamma(\omega)]$, $\mathrm{Im}[\beta(\omega)]$ at constant $\mathrm{Re}[\gamma(\omega)]$, $\mathrm{Re}[\beta(\omega)]$ using a root-finding algorithm for a set of nonlinear equations. The domination of the optical response of metal particles by absorption supports the choice of solving the system of equations at constant real part (see the long-wavelength limit Eq. 5). The inversion proceeds iteratively from a given spectral range; at each iteration, $\mathrm{Re}[\gamma(\omega)]$, $\mathrm{Re}[\beta(\omega)]$ are calculated by KK relations (Eq. 6) and used as input to the next step. The process ends when the sought quantities are stable enough. To insure a better convergence, $\mathrm{Im}[\gamma(\omega)]$, $\mathrm{Im}[\beta(\omega)]$ are increased only by a given amount along the expected gradients at each step instead of being set to the roots of the system of equations (3–4). This forces $\mathrm{Im}[\gamma(\omega)]$, $\mathrm{Im}[\beta(\omega)]$ to keep KK consistent with $\mathrm{Re}[\gamma(\omega)]$, $\mathrm{Re}[\beta(\omega)]$ [37] at each iteration. Root-finding is performed with Brown's variation of Newton's method (`SLATEC` numerical library http://www.netlib.org/slatec/). The Cauchy principal part is calculated through trapezoidal integration since signals and dielectric constants are cubic spline interpolated on equally spaced energy abscissa. This reverts to a discrete KK transform [43]; similar accuracy was obtained with conjugate Fourier series approach [55]. A further advantage for the convergence is brought in the analysis of actual experiments by the continuous recording of data and their inversion as a function of time; the inverted IS of each spectrum is used as input for the next analysis.

However, a crucial issue in the KK transform of experimental data [41] is the finite wavelength/energy bandwidth $[\omega_1, \omega_2]$, whereas Eq. 6 are valid only for an infinite integration range. A residual part $\mathrm{Re}[\gamma_r(\omega), \beta_r(\omega)]$ of the total signal $\mathrm{Re}[\gamma(\omega), \beta(\omega)]$ is lacking in the measurements because of the inherent nonlocal character of the KK transform:

$$\begin{aligned} \mathrm{Re}[\gamma(\omega), \beta(\omega)] &= \mathrm{Re}[\gamma_r(\omega), \beta_r(\omega)] \\ &\quad + \frac{2}{\pi}\wp\int_{\omega_1}^{\omega_2} d\omega' \frac{\omega' \mathrm{Im}[\gamma(\omega'), \beta(\omega')]}{\omega'^2-\omega^2} \end{aligned} \tag{7}$$

In general, this term results from tails of external lying absorption thresholds in the imaginary part of the dielectric constants, from either the particle itself or indirectly excited in the substrate by particle polarization, or tails of plasmon modes peaking outside the probed frequency range. $\mathrm{Re}[\gamma_r(\omega), \beta_r(\omega)]$ terms must be accounted for to avoid

bias of the inversion algorithm of the reflection coefficients towards unphysical solutions with negative imaginary part. To partially avoid edge effects in the calculation of the integral in Eq. 6, Im[$\gamma(\omega)$], Im[$\beta(\omega)$] were extrapolated using a low-order polynomial fit (second order in general) over limited windows at both edges (typically 0.5 eV). Although useful for KK transform close to the boundaries ω_1, ω_2, this does not cure the problem. At best, if the probed range encompasses most of the resonant behavior as in the case of plasmon excitations in noble metal particles, the residual term can be approximated by a constant offset independent of the frequency Re[γ_0, β_0] which cannot be neglected.

To cope with the issue, the SDRS data were fitted to the spheroidal dipole approximation (SDA) [3, 48], a light method that was preferred to more realistic but demanding approaches [3] based on interacting truncated spheres [6, 7, 29, 33, 56] or truncated oblate or prolate spheroids [30]. In SDA, the particle is assumed to be a full spheroid sitting on the substrate (Fig. 1). Its polarizability is obtained by solving the Laplace equation up to dipolar order. Compared to multipolar calculations, SDA [3, 48] leads to more accurate depolarization factors than Yamaguchi's model [3, 48, 57, 58] that corrects the unsupported full spheroid dipole behavior only from image field. However, despite the flexibility of the model in terms of aspect ratio, the full spheroid shape and the restriction to dipolar order of the electrostatic coupling with the substrate unable SDA to reproduce quantitatively the multipolar modes excited by particle truncation and image fields [31, 32, 34, 35] and to feature correctly particle morphology [33, 56]. Nevertheless, for sharp plasmon peaks, SDA is expected to grasp most of the "smoother" dielectric contribution of Re[$\gamma_r(\omega)$, $\beta_r(\omega)$] in the spectral range under study [49, 50]. On a practical point of view, to recover an estimate of Re[$\gamma_r(\omega)$, $\beta_r(\omega)$], particles (Fig. 1) are modeled by a hexagonal lattice (parameter L) of oblate spheroids with revolution axis normal to the substrate that interact through dipole–dipole coupling. Their parallel $D_\parallel = 2a\sqrt{1+\xi_0^2}$ and perpendicular $H_z = 2a\xi_0$ diameters are function of the flattening parameter ξ_0 ($1 < \xi_0 < +\infty$) and of the size of ring of foci a of the ellipsoidal shape. The spheroid center O is located at a distance $d = a\xi_1$ from the substrate surface $z = 0$, and its aspect ratio is defined through $\mathcal{A}_{r,S} = D_\parallel / H_z$. As shown in Appendix, the polarizabilities and corresponding IS (γ_S, β_S) are analytic function of the geometrical parameters (a, ξ_0, ξ_1, L) and dielectric constants $\epsilon, \epsilon_1, \epsilon_2$ for particle, embedding medium and substrate, respectively. To mimic the inhomogeneous broadening due to size/shape distributions in real samples, the IS can be folded with Gaussian of widths $\sigma_\parallel, \sigma_z$ which proved to be satisfactory even for quantitative analysis [6, 7, 26, 33]:

$$\gamma_S(\omega), \beta_S(\omega) = \frac{1}{\sigma_{\parallel,z}\sqrt{2\pi}} \int_{\omega_1}^{\omega_2} \alpha_{S\parallel,z}(\omega') e^{-(\omega'-\omega)/2\sigma_{\parallel,z}^2} d\omega' \tag{8}$$

Once fitted to SDRS data through formulae Eqs. 3–4, the SDA γ_S, β_S are used to estimate the residual term through the following equation:

$$\mathrm{Re}[\gamma_r(\omega), \beta_r(\omega)] \simeq \mathrm{Re}[\gamma_S(\omega), \beta_S(\omega)] - \frac{2}{\pi} \wp \int_{\omega_1}^{\omega_2} d\omega' \frac{\omega' \mathrm{Im}[\gamma_S(\omega'), \beta_S(\omega')]}{\omega'^2 - \omega^2} \tag{9}$$

In some cases, for films close to percolation, a way to improve the fits is to add to the spheroid model a thin film behavior following Eq. 1.

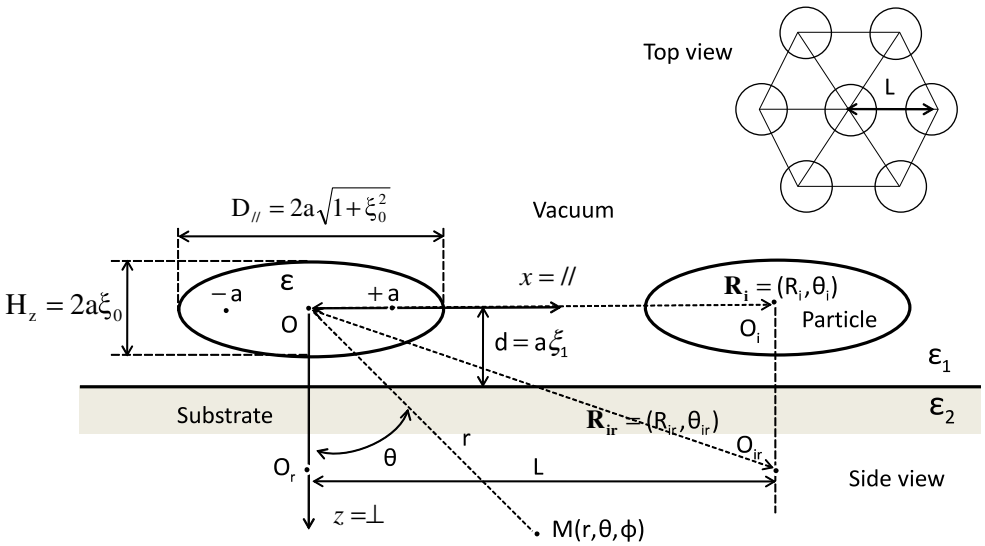

Fig. 1 Oblate spheroid morphology used as the starting point of the inversion algorithm (see text). The particles of parallel diameter $D_\parallel$ and height H_z (or perpendicular diameter) have a revolution axis along the z-direction perpendicular to the substrate and are organized on a perfect hexagonal lattice. Their centers sit at a distance d from the substrate. $\mathcal{O}$ and $\mathcal{O}_r$ stand for the position of the direct and image points

Inversion Tests on Synthetic Differential Reflectivity Data

The inversion algorithm was tested on synthetic data obtained with the `GranFilm` software [56] for silver and gold on alumina (Al_2O_3), zincite (ZnO), and titania (TiO_2). The Ag and Au metals are test beds for plasmonic excitations [47] with a Drude behavior poorly damped by interband transitions [59]. Alumina is an archetype of non-absorbing wide bandgap material, while zincite and titania represent a semiconducting behavior that is characterized by a bandgap located in the UV–visible range with a threshold of absorption close to 3 eV (Fig. 2).

Synthetic Data of SDRS: Limits of Long-Wavelength Approximation and SDA Fits

The model system to calculate SDRS synthetic data was a layer of truncated spheres (see Fig. 2 of ref. [33] for definitions) of diameter $D = 8$ nm packed on an hexagonal lattice of parameter $L = 12$ nm leading to surface coverage $\Theta = \rho\pi D^2/4 = \frac{\pi D^2}{2\sqrt{3}L^2} = 40\ \%$ and an average film thickness of $t = 1.92$ nm. The particle aspect ratio $\mathcal{A}_r = \frac{D}{H} = \frac{2}{1+t_r}$ (in-plane diameter/height) was fixed at $\mathcal{A}_r = 1.25$ (truncation $t_r = 0.6$) giving a contact angle $\theta_c = \arccos(-t_r) = 126°$ which, typical for noble metals on wide bandgap oxides [60], corresponds to Ag/alumina at equilibrium [6, 24, 33]. Polarizabilities $\alpha_\parallel, \alpha_z$ and corresponding IS (Eq. 2) were determined in the quasi-static approximation by means of a multipole expansion technique [3, 29–31, 33, 61]. A satisfactory convergence was achieved at a multipolar order of $M = 24$. Polarizabilities were then renormalized by particle–particle interaction at dipolar order. No finite-size correction was applied to the bulk interpolated dielectric constants from ref. [62] (Fig. 2). Media were made optically isotropic by averaging if necessary.

Frameworks of calculation of the reflection coefficients are compared for Ag/Alumina in Fig. 3: (i) IS of first-order

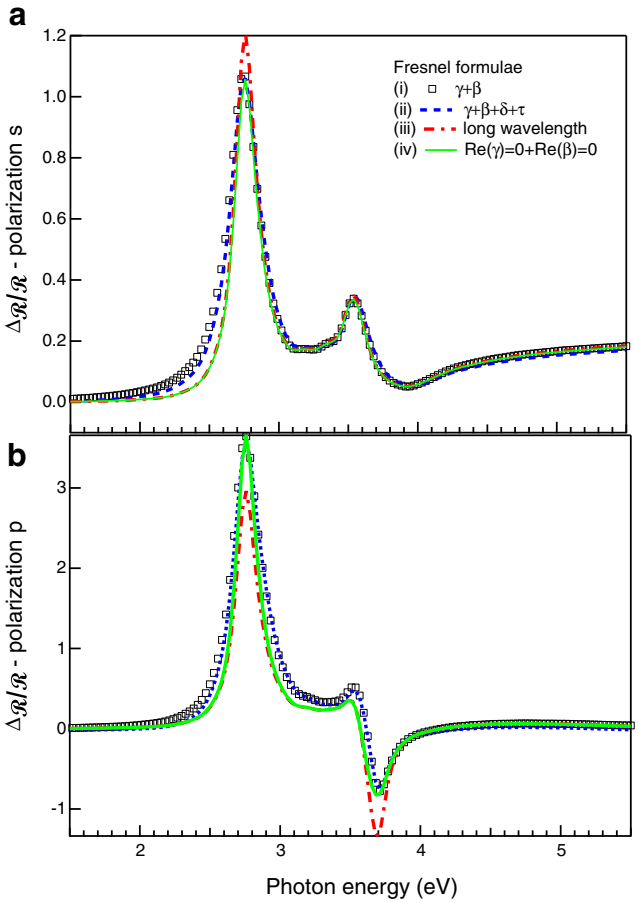

Fig. 3 Synthetic surface differential reflectivity spectra for silver particles of 8 nm in diameter that are represented by truncated spheres (aspect ratio $\mathcal{A}_r = D/H = 1.25$; contact angle $\theta_c = 126°$) supported on alumina in **a** $s-$polarization and **b** $p-$polarization within different frameworks: (*i*) only the first-order IS ($\gamma + \beta$), (*ii*) all the susceptibilities of first ($\gamma + \beta$) and second order ($\delta + \tau$), (*iii*) the long-wavelength approximation (Eq. 5), and (*iv*) Eqs. 3–4 where the real part of the IS is set to zero

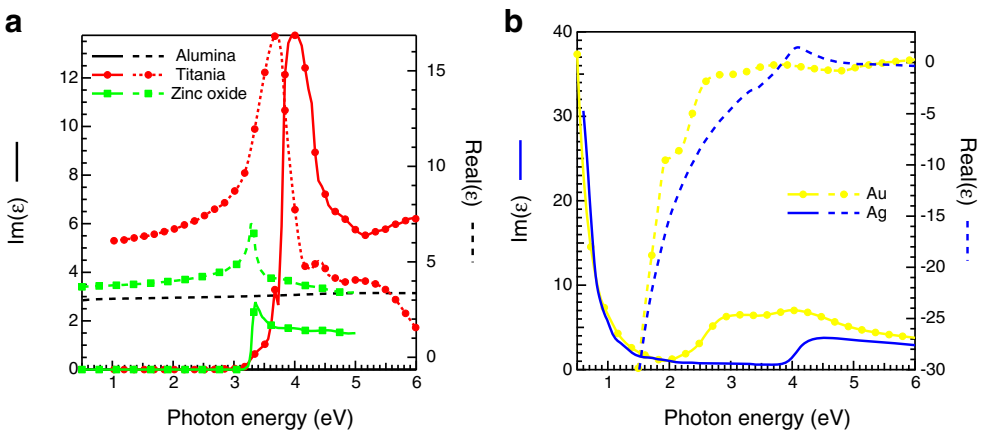

Fig. 2 Dielectric constants used herein for **a** the oxide substrates and **b** the metallic films. *Full lines*, real parts; *dashed lines*, imaginary parts. From ref. [62]

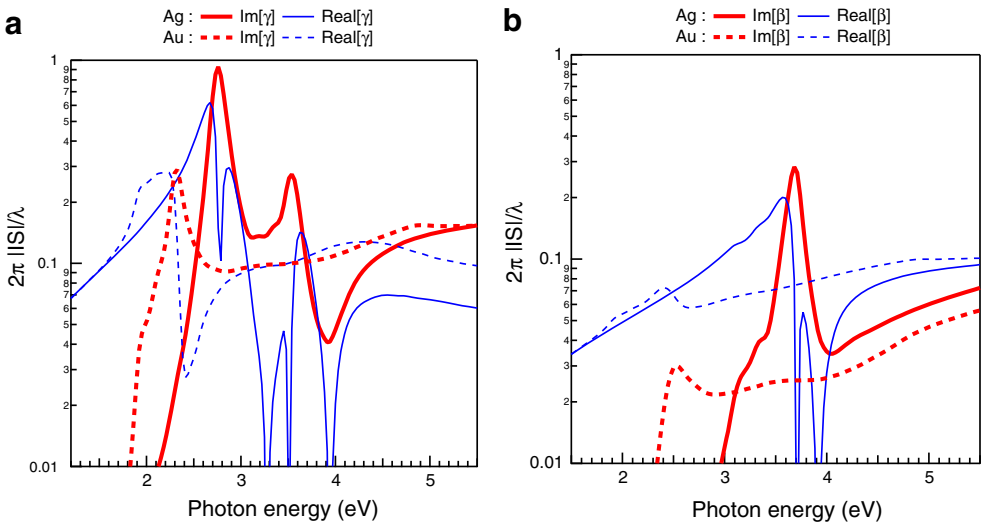

Fig. 4 Silver and gold on alumina: Check of the long-wavelength approximation for silver and gold supported on alumina for the IS corresponding to the SDRS spectra of Fig. 5: **a** $2\pi/\lambda|\mathrm{Im}(\gamma)|$ and $2\pi/\lambda|\mathrm{Re}(\gamma)|$ and **b** $2\pi/\lambda|\mathrm{Im}(\beta)|$ and $2\pi/\lambda|\mathrm{Re}(\beta)|$

γ, β only (Eqs. 3–4), (ii) IS of all orders $\gamma, \beta, \delta, \tau$, (iii) long-wavelength approximation (Eq. 5), and (iv) Eqs. 3–4 where the real parts of the IS are neglected. Fresnel expressions including second-order interfacial susceptibilities δ, τ which are linked to the static particle quadrupole polarizabilities can be found in refs. [3, 19]. Firstly, for metallic particles, the second-order IS δ, τ have a minute effect on a signal dominated by plasmon absorption which confirms that they can be neglected [19] (Fig. 3 (i, ii)). Conversely, in SDRS spectra mostly driven by the imaginary parts of the IS, the contribution of the real terms remains sizable (Fig. 3 (iv)). Finally, the failure of the long-wavelength approximation to reproduce accurately both widths and intensities of peaks (Fig. 3 (iii)) shows the limit of the hypothesis $2\pi|\gamma, \beta|/\lambda \ll 1$. As illustrated in Fig. 4 for Ag and Au on alumina, this quantity can be much higher than 10 % even for nanometric-sized ($D = 8$ nm herein) particles because of the strong plasmonic resonances. Originally derived by McIntyre and Aspnes [5] from a long-wavelength expansion of the thin plate model, Eq. 5 were extended by Dignam and Moskovits to anisotropic layer [13, 14]. Although appealing in terms of physical meaning, these equations are to be used cautiously for quantitative analysis since γ, β can reach values as high as several tens of nanometres (see next sections). In what follows, calculations and inversions are based only on Eqs. 3–4.

Notably, there exists a good apparent agreement between synthetic SDRS data and SDA fits (Figs. 5–6). However, it systematically requires strong distortions in the morphology of the supported clusters. Silver and gold particles supported on alumina are flatter (the spheroid aspect ratio is $\mathcal{A}_{r,S} = 2$ instead of $\mathcal{A}_r = 1.26$ for the initial truncated sphere), films are thinner ($t_S = 1$ nm instead of $t = 1.92$ nm), and, more strikingly, spheroids are partially buried with $d < H_z/2$ although it is not allowed in the modeling. Regarding supported silver (Fig. 5a), the shoulder at 3.5 eV previously assigned to a quadrupole-like mode [31, 32] is not accounted for. In the case of silver on zinc oxide and gold on titanium oxide (Fig. 6), the qualitative agreement of SDA with synthetic data hides similar discrepancies. Particles are even flatter ($\mathcal{A}_{r,S} \simeq 2.6$), films much thinner ($t_S \simeq 0.7$ nm), and coverages much lower ($\simeq 10$ % instead of $\simeq 40$ %) with partially buried spheroids. These examples highlight the pitfalls which result from

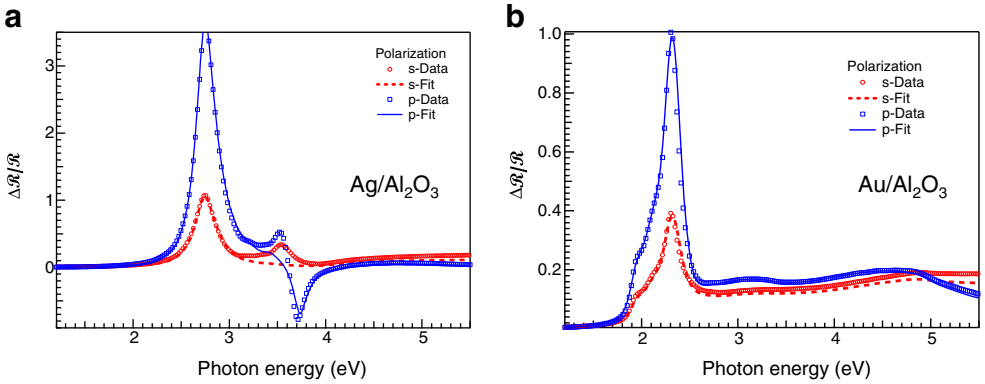

Fig. 5 Fit of the $D = 8$ nm truncated sphere synthetic SDRS spectra with the spheroidal dipole approximation (SDA): **a** silver on alumina and **b** gold on alumina. The discrepancies between synthetic data and SDA model are discussed in the text

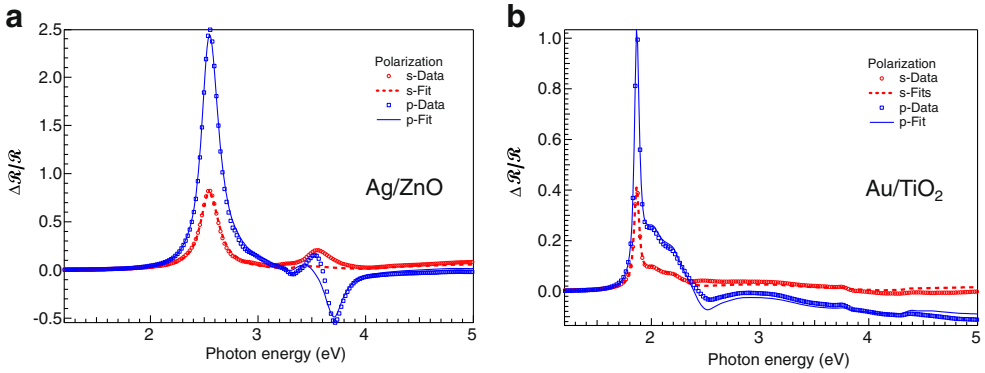

Fig. 6 Same as Fig. 5. **a** Silver on zincite. **b** Gold on titania. The discrepancies between synthetic data and SDA model are discussed in the text

the use of "basic modeling" [48, 57, 58] for a quantitative description.

Nonabsorbing Substrates: Silver and Gold on Alumina

However, although not appropriate for the modeling of the optical response as a whole, SDA was quite successful in fitting the synthetic SDRS signals $\Delta\mathcal{R}_s/\mathcal{R}_s$, $\Delta\mathcal{R}_p/\mathcal{R}_p$ obtained from Eqs. 3–4 to derive estimates of the residual terms γ_r, β_r prior to inversion.

Results of the inversion process are presented for silver and gold on alumina in Figs. 7 and 8, respectively. Calculations of IS from synthetic data, IS from SDA fit, and IS from inversion of SDRS spectra with and without SDA residual terms are compared. Without residual terms, the inversion can be biased towards negative values of Im(β) for silver, while for gold, the imaginary parts of IS are overestimated outside the plasmon peak. In addition, the real parts of IS are strongly underestimated except for the Re(γ) term of silver which shows a slighter discrepancy. Adding the SDA residual term much improves the quality of the inversion results. Most importantly, the imaginary parts are correctly extracted. A nearly constant offset is still missing on the real part, but it is difficult to derive accurately these terms whose contribution is relatively small. The case of gold highlights the interest of the inversion since, unlike silver (Fig. 5a), parallel γ and perpendicular β susceptibility contributions are completely entangled in the SDRS spectra (Fig. 5b) while they are clearly separated by inversion. The tests made herein are quite stringent since the IS have values (up to 60 nm) much higher than the weighted thickness of the film $t = 1.94$ nm. Moreover, as

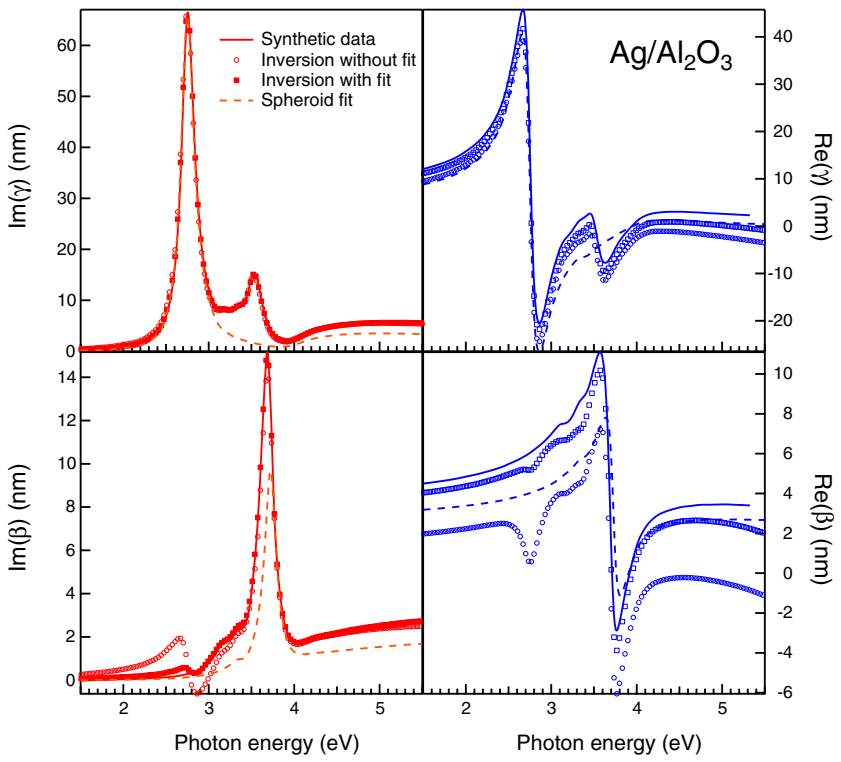

Fig. 7 Inversion results of the synthetic SDRS spectra for silver on alumina: the initial IS data from `GranFilm` (*full lines*); IS from fits of SDRS data in the SDA framework (*dashed lines*. Note the strong discrepancies with synthetic data); inversion without (*circles*) or with (*square*) the use of SDA model to estimate residual terms in the Kramers–Kronig integration. The latter is seen to much improve the quality of the inversion for the imaginary and real parts of the perpendicular IS (β)

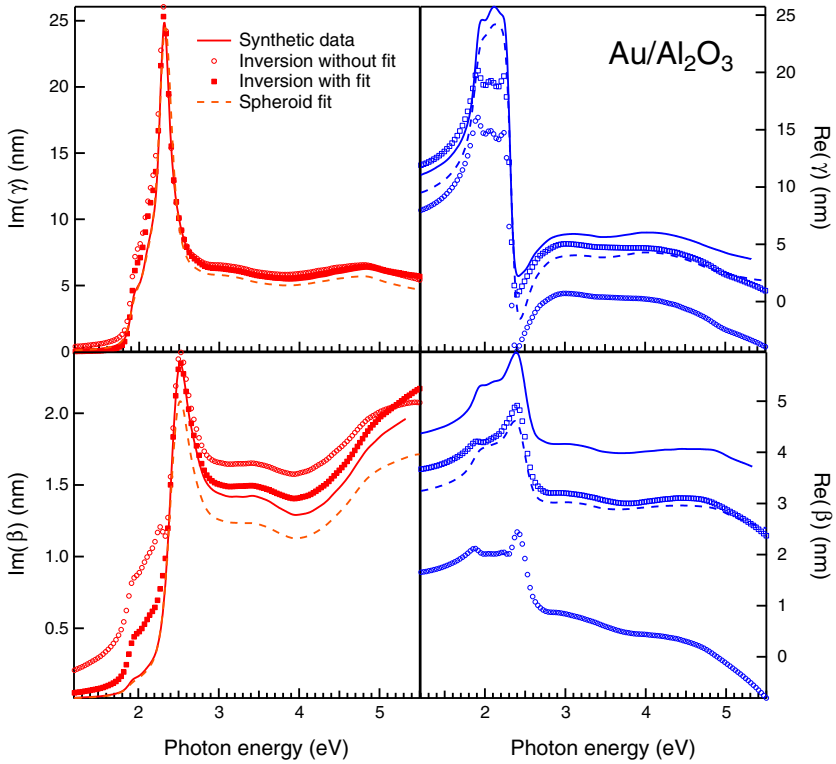

Fig. 8 Gold on alumina: same as Fig. 7. The use of SDA strongly improves the inversion for the real part of γ and the real and imaginary parts of β

already noticed in the direct fitting of experimental data [6, 33] with truncated sphere, $D \simeq 8$ nm was an upper limit above which the agreement between experiments and theory becomes poorer. Indeed, even better inversion results are obtained for smaller particles (not shown) as the reflectivity gets closer to the long-wavelength approximation.

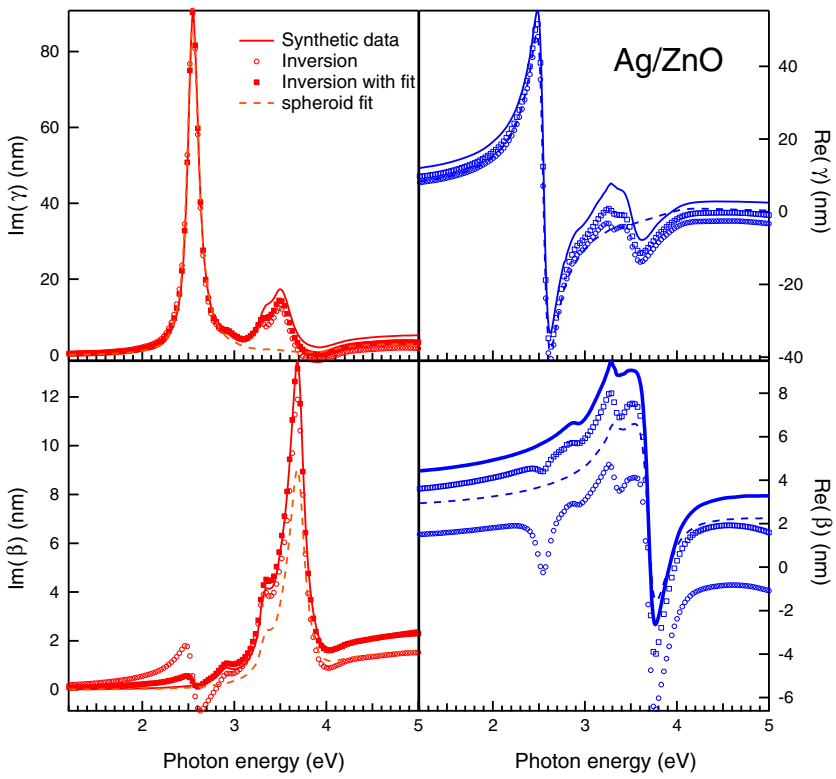

Fig. 9 Silver on zincite: same as Fig. 7

Semiconducting Substrates: Silver on Zincite and Gold on Titania

The question which rises up now is the validity of the inversion in the case of absorbing substrates with a semiconducting behavior. Two systems were studied, Ag/ZnO and Au/TiO_2. The use of the fitted residual terms γ_r, β_r does improve the inversion process as seen in Figs. 9–10. The extraction of IS is as good in the case of Ag/ZnO as it is for Ag/Al_2O_3 even close to the bandgap. The success of the method can be related to the moderate value of the dielectric function of zincite. The inversion is slightly less satisfactory for Au/TiO_2, regarding in particular the real contributions. The strong resonance of Im(γ) induces a nonphysical negative Im(β) at the same frequency which is cured by adding the proper fitted offset. However, Re(β) is underestimated, while Re(γ) and Im(γ) present a wrong feature at onset of titania absorption threshold. The Au/titania case encounters a series of difficulties: (a) the spectral intertwining of the IS, (b) the strength and structure of the dielectric function of the substrate which enhance considerably the gold plasmon peak close to 2 eV compared to alumina, and (c) the huge discrepancy between parallel and perpendicular IS. Other tests made with Ag/TiO_2 or Ag/Si, the latter substrate having an even higher and more structured dielectric function in the UV domain, lead to similar conclusions. Despite those drawbacks, the main components involved in the plasmonic response of the two metals (Au and Ag) along the directions parallel and perpendicular to the substrate are always well recovered. For instance, the structures which appear at 3.5 eV for silver on zincite (Fig. 9) or 2.5 eV for gold on titania (Fig. 10) are clearly disentangled from SDRS spectra. This paves the way to their identification in actual experiments.

Conclusions and Outlook

An algorithm was set up to derive the parallel and perpendicular interfacial susceptibilities that characterize the optical response of supported metallic nanoparticles. It is based on inversion of the reflection coefficients for two polarization states *s* and *p* and KK analysis. In order to calculate the KK integrals over a limited energy domain, the strategy was to complement the data in the UV–visible energy range by spectra calculated in the framework of the SDA, although the SDA alone is shown not to be appropriate to quantitatively model supported films. The algorithm has been successfully tested on SDRS for nanoparticles of silver and gold in an energy range where optical responses are dominated by plasmonic excitations with a noticeable Drude behavior, these particles being supported on either nonabsorbing wide bandgap Al_2O_3 or semiconducting zincite ZnO or titania TiO_2. The algorithm was shown to allow recovering IS features hidden in the reflectivity measurements. Moreover, it was evidenced that sizable plasmon

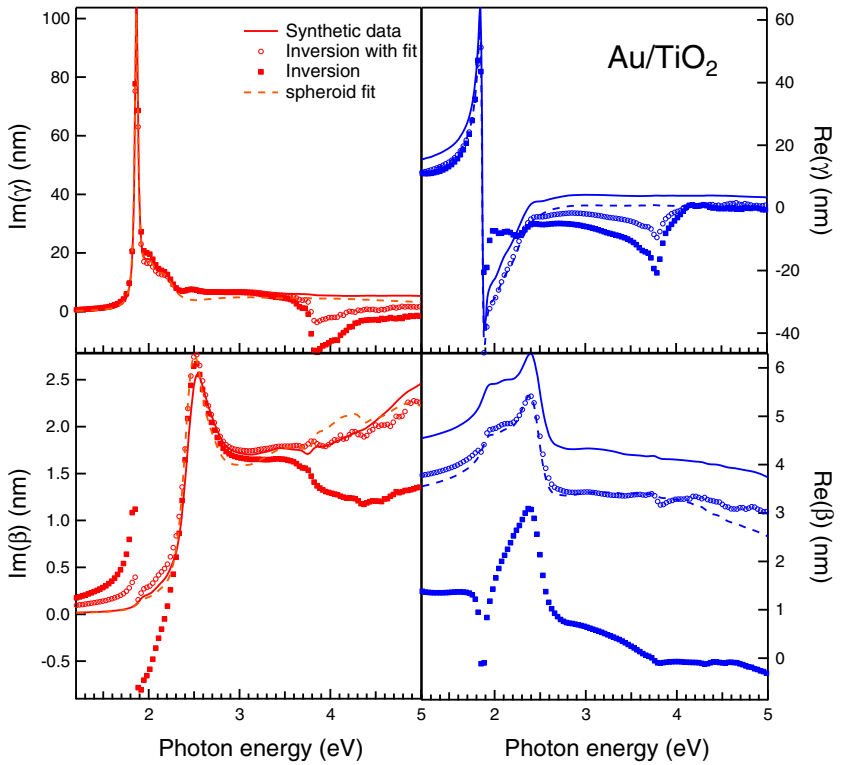

Fig. 10 Gold on titania: same as Fig. 7

resonances prevent the use of the classical long-wavelength dielectric approximation even for nanometric-sized objects. Provided moderate substrate dielectric constants and spectral range which encompasses most of the resonant plasmonic behavior, the present work could be generalized to (a) other morphologies beyond the case of supported nanoparticles as well as to (b) other combinations of optical coefficients. Examples are the cases of (a) rough thin films or surfaces for which basic models of IS exist [3] to estimate the residual terms and (b) of ellipsometric coefficients. The application of the algorithm to SDRS measurements during metal/oxide growth will be the topics of a forthcoming paper (Lazzari et al. 2013, submitted).

Acknowledgments This work has been funded by Agence Nationale de la Recherche (ANR) (Program "Matériaux et Procédés pour des Produits Performants" contract ANR-2011-RMNP-010, COCOTRANS) and has benefited from a mobility grant AURORA between France and Norway.

Appendix: Supported Spheroid Polarizability in the Spheroidal Dipole Approximation

The aim of this appendix is to recall the expressions of the supported spheroid depolarization factors which are used as starting point of the inversion algorithm of SDRS. The geometry will be restricted to an oblate spheroid as it better describes the experimental particle flattening. Electrostatic interactions, both with the substrate and between particles, are kept at dipolar order for the sake of simplicity. Particles are ordered on a lattice of parameter L. Anyhow, equations for prolate case and up to the quadrupolar order can be easily found in the literature [3]. All the geometrical parameters are defined in the text and in Fig. 1.

The derivation of spheroid polarizabilities was obtained by Bobbert and Vlieger [3, 48, 56]; the Laplace equation is solved by using a multipolar spheroidal expansion [63] of the potential located both at the centers $\mathcal{O}$ and at the image $\mathcal{O}_r$ points in the substrate for all the spheroids. The continuity of the potential and of the normal derivative of the displacement field at the surface of the spheroids leads to an infinite set of linear equations for the spheroidal multipole coefficients. Once restricted to dipole interaction, the particle polarizability reads as follows:

$$\begin{aligned}\alpha_{S,z} &= \epsilon_1 V \frac{\epsilon-\epsilon_1}{\epsilon_1+L_z(\epsilon-\epsilon_1)}\\ \alpha_{S,\parallel} &= \epsilon_1 V \frac{\epsilon-\epsilon_1}{\epsilon_1+L_\parallel(\epsilon-\epsilon_1)}\end{aligned} \tag{10}$$

where $V = 4/3\pi a^3\xi_0(1+\xi_0^2)$ is the spheroid volume. The depolarizations factors are given by

$$\begin{aligned}L_z &= (1+\xi_0^2)\left\{1-\xi_0\arctan\left(\frac{1}{\xi_0}\right)-\left(\frac{\epsilon_1-\epsilon_2}{\epsilon_1+\epsilon_2}\right)\xi_0\Xi(\xi_1)-\frac{V}{L^3(1+\xi_0^2)}\Sigma_{20}^-\right\}\\ L_\parallel &= \frac{1}{2}(1+\xi_0^2)\left\{\xi_0\arctan\left(\frac{1}{\xi_0}\right)-\frac{\xi_0^2}{1+\xi_0^2}-\left(\frac{\epsilon_1-\epsilon_2}{\epsilon_1+\epsilon_2}\right)\xi_0\Xi(\xi_1)+\frac{V}{L^3(1+\xi_0^2)}\Sigma_{20}^+\right\}\\ \Xi(\xi_1) &= \left(\frac{3}{2}+\xi_1^2\right)\xi_1\ln\left(1+\frac{1}{\xi_1^2}\right)-\arctan\left(\frac{1}{\xi_1}\right)-\xi_1\\ \Sigma_{20}^\pm &= \frac{1}{\sqrt{5\pi}}\left[S_{20}\pm\left(\frac{\epsilon_1-\epsilon_2}{\epsilon_1+\epsilon_2}\right)\widetilde{S}_{20}^r\right]\end{aligned} \tag{11}$$

The dipole–dipole interaction between particles comes into play through the lattice sums (S_{20}, S_{20}^r) over the direct $\mathbf{R}_i$ and image $\mathbf{R}_i^r$ points. They are defined through the following:

$$S_{20}=\sum_{i\neq0}\left(\frac{L}{r}\right)^3 Y_2^0(\theta,\phi)\Big|_{\mathbf{r}=\mathbf{R}_i}=-\frac{1}{4}\sqrt{\frac{5}{\pi}}\sum_{i\neq0}\left(\frac{L}{R_i}\right)^3 \tag{12}$$

$$S_{20}^r=\sum_{i\neq0}\left(\frac{L}{r}\right)^3 Y_2^0(\theta,\phi)\Big|_{\mathbf{r}=\mathbf{R}_i^r}=\frac{1}{4}\sqrt{\frac{5}{\pi}}\sum_{i\neq0}\left(\frac{L}{R_i^r}\right)^3\times\left(3\cos^2\theta_i^r-1\right) \tag{13}$$

where $Y_2^0(\theta,\phi)$ is the spherical harmonics of order $\ell = 2, m = 0$. They depend on the spherical angle from direct (θ,ϕ) or image (θ^r,ϕ^r) points (Fig. 1). The sums are calculated using the convergence trick of ref. [64]. The IS in the spheroidal dipole approximation are related to the above polarizabilities through the following:

$$\gamma=\rho\alpha_{S,\parallel},\quad \beta=\rho\alpha_{S,z} \tag{14}$$

where ρ is the number of particles per surface unit.

References

1. Stockman M (2011) Phys Today 64:39

2. Kreibig U, Vollmer M (1995) Optical properties of metal clusters, vol 25. Springer, Berlin
3. Bedeaux D, Vlieger J (2001) Optical properties of surfaces. Imperial College Press, London
4. Noguez C (2007) J Phys Chem 111:3806
5. McIntyre J, Aspnes D (1971) Surf Sci 24:417
6. Lazzari R, Jupille J (2012) Nanotechnology 23:135707
7. Grachev S, de Grazia M, Barthel E, Søndergård E, Lazzari R (2013) J Phys D Appl Phys 46:375305. 10pp
8. Oates T, Christalle E (2007) J Phys Chem C 111:182
9. Larsson E, Langhammer C, Zorić I, Kasemo B (2009) Science 326:1091
10. Gaudry M, Cottancin E, Pellarin M, Lermé J, Arnaud L, Huntzinger JR, Vialle JL, Broyer M, Rousset JL, Treilleux M, Mélinon P (2003) Phys Rev B 67:155409
11. Little SA, Begou T, Collins RW, Marsillac S (2012) Appl Phys Lett 100:051107
12. Drude P (1902) The theory of optics. Longmans, Green and Co, New York
13. Dignam M, Moskovits M, Stobie R (1971) Trans Faraday Soc 67:3306
14. Dignam M, Moskovits M (1973) J Chem Soc Faraday Trans II 69:56
15. Bagchi A, Barrera RG, Rajagopal AK (1979) Phys Rev B 20(12):4824
16. Feibelman PJ (1982) Prog Surf Sci 12:287
17. Hugerl K, Aspnes DE, Kamiya I, Florez LT (1993) Appl Phys Lett 63:885
18. Bedeaux D, Vlieger J (1973) Physica 67:55
19. Haarmans M, Bedeaux D (1995) Thin Solid Films 258:213
20. Proehl H, Nitsche R, Dienel T, Leo K, Fritz T (2005) Phys Rev B 71:165207
21. Pollak FH, Shen H (1993) Mat Sci and Eng 10:275
22. Hummel RE (1983) Phys Stat Sol 76:11
23. Borensztein Y, Abelès F (1985) Thin Solid Films 125:129
24. Lazzari R, Jupille J (2005) Phys Rev B 71:045409
25. Camacho-Flores J, Sun L, Saucedo-Zeni N, Weidlinger G, Hohage M, Zeppenfeld P (2008) Phys Rev B 78:075416
26. Lazzari R, Renaud G, Revenant C, Jupille J, Borenstzein Y (2009) Phys Rev B 79:125428
27. Debe MK (1987) Prog Surf Sci 24:1
28. Proehl H, Dienel T, Nitsche R, Fritz T (2004) Phys Rev Lett 93:097403
29. Simonsen I, Lazzari R, Jupille J, Roux S (2000) Phys Rev B 61(11):7722
30. Lazzari R, Simonsen I, Bedeaux D, Vlieger J, Jupille J (2001) Eur Phys J B 24:267
31. Lazzari R, Roux S, Simonsen I, Jupille J, Bedeaux D, Vlieger J (2002) Phys Rev B 65:235424
32. Lazzari R, Simonsen I, Jupille J (2003) Europhys Lett 61ll (4):541
33. Lazzari R, Jupille J (2011) Nanotechnology 22:445703
34. Beita C, Borensztein Y, Lazzari R, Nieto J, Barrera R (1999) Phys Rev B 60(8):6018
35. Román-Velázquez CE, Noguez C, Barrera RG (2000) Phys Rev B 61(15):10427
36. Lazzari R, Layet JM, Jupille J (2003) Phys Rev B 68:045428
37. Nitsche R, Fritz T (2004) Phys Rev B 70:195432
38. Henrichs S, Collier CP, Saykally RJ, Shen YR, Heath JR (2000) J Am Chem Soc 122:4077
39. Poelman D, Smet PF (2003) J Phys D Appl Phys 36:1850
40. Shiles E, Sasaki T, Inokuit M, Smith DY (1980) Phys Rev B 22:1612
41. Smith D (1985) Dispersion theory, sum rules and their applications in the analysis of optical data. In: Handbook of optical constants of solids, vol 1. Academic, New York, pp 35–64
42. Prange RE, Drew HD, Restorffg JB (1977) J Phys C Sol Stat Phys 10:5083
43. Moreels I, Allan G, De Geyter B, Wirtz L, Delerue C, Hens Z (2010) Phys Rev B 81:235319
44. Ahrenkiel R (1971) J Opt Soc Am 61:1651
45. Palmer K, William M, Budde B (1998) Appl Opt 37:2660
46. Kuzmenko A (2005) Rev Sci Inst 76:083108
47. Bohren CF, Huffman DR (1983) Absorption and scattering of light by small particles. Wiley, New York
48. Bobbert PA, Vlieger J (1987) Physica A 147:115
49. Wormeester H, Kooij S, Poelsema B (2003) Phys Rev B 68:085406
50. Wormeester H, Henry AI, Kooija ES, Poelsema B, Pileni MP (2006) J Chem Phys 124:204713
51. Albano AM, Bedeaux D, Vlieger J (1979) Physica A 99:293
52. Albano AM, Bedeaux D, Vlieger J (1980) Physica A 102:105
53. Bedeaux D, Vlieger J (1973) Physica A 73:287
54. Vlieger J, Bedeaux D (1980) Thin Solid Films 69:107
55. King F (1978) J Opt Soc. Am 68:994
56. Lazzari R, Simonsen I (2002) Thin Solid Films 419:124
57. Yamaguchi T, Yoshida S, Kinbara A (1973) Thin Solid Films 18:63
58. Yamaguchi T, Yoshida S, Kinbara A (1974) Thin Solid Films 21:173
59. Johnson P, Christy R (1972) Phys Rev B 6:4370
60. Campbell CT (1997) Surf Sci Rep 27(1–3):1
61. Wind MM, Vlieger J (1987) Physica A 141:33
62. Palik ED (1985) Handbook of optical constants of solids, vol. 1–3. Academic, New York
63. Jackson JD (1975) Classical electrodynamics. Wiley, New York
64. Haarmans MT, Bedeaux D (1993) Thin Solid Films 224:117